Solution of the time-harmonic viscoelastic inverse problem with interior data in two dimensions

Yixiao Zhang[1], Assad A Oberai[1,*,†], Paul E Barbone[2] and Isaac Harari[3]

[1]*Mechanical Aerospace and Nuclear Engineering, Rensselaer Polytechnic Institute, Troy, NY, USA*
[2]*Mechanical Engineering, Boston University, Boston, MA, USA*
[3]*Faculty of Engineering, Tel Aviv University, Ramat Aviv, Tel Aviv, Israel*

SUMMARY

We consider the problem of determining the distribution of the complex-valued shear modulus for an incompressible linear viscoelastic material undergoing infinitesimal time-harmonic deformation, given the knowledge of the displacement field in its interior. In particular, we focus on the two-dimensional problems of anti-plane shear and plane stress. These problems are motivated by applications in biomechanical imaging, where the material modulus distributions are used to detect and/or diagnose cancerous tumors. We analyze the well-posedness of the strong form of these problems and conclude that for the solution to exist, the measured displacement field is required to satisfy rather restrictive compatibility conditions. We propose a weak, or a variational formulation, and prove the existence and uniqueness of solutions under milder conditions on measured data. This formulation is derived by weighting the original PDE for the shear modulus by the adjoint operator acting on the complex-conjugate of the weighting functions. For this reason, we refer to it as the complex adjoint weighted equation (CAWE). We consider a straightforward finite element discretization of these equations with total variation regularization, and test its performance with synthetically generated and experimentally measured data. We find that the CAWE method is, in general, less diffusive than a corresponding least squares solution, and that the total variation regularization significantly improves its performance in the presence of noise. Copyright © 2012 John Wiley & Sons, Ltd.

1. INTRODUCTION

Recent developments in imaging technology have made it possible to determine the displacement field in the interior of tissue in response to a dynamic excitation [1–3]. This is typically accomplished using MRI or ultrasound. When MRI is used, the excitation is at a fixed frequency, and thus the time-harmonic response of the tissue is measured. On the other hand, when ultrasound is used, the excitation is dynamic and broad-band. However, even in this case, the dynamic displacement field is often resolved into its time-harmonic components via a Fourier transform. The time-harmonic displacement in the *interior* of the tissue offers a wealth of information that may be used to characterize its material properties. In particular, it may be used to determine the spatial variation of its viscoelastic properties by solving an inverse problem. These properties in turn carry information about the tissue microstructure and pathology. For example, it is well recognized that cancerous tumors tend to be stiffer than their surroundings because of the recruitment of collagen

---

*Correspondence to: Assad A Oberai, Mechanical Aerospace and Nuclear Engineering, Rensselaer Polytechnic Institute, Troy, NY, USA.

†E-mail: oberaa@rpi.edu

during tumorigenesis [4]. This has been verified in *ex vivo* mechanical tests of breast tissue samples [5]. Thus creating images of the stiffness of tissue may aid in the detection and diagnosis of cancer.

There has been substantial work devoted to solving the time-harmonic inverse elasticity problem. In the algebraic inversion approach [6], the pressure field in the equations is ignored and an assumption of local homogeneity is made. This yields three algebraic equations for the shear modulus at each spatial location, which are solved in a least-squares sense. In the curl-based algebraic inversion method [3], the pressure is first eliminated by taking the curl of the equations of motion, and then material homogeneity is invoked. This also yields an algebraic set of equations for the spatial distribution of the shear modulus. However, the operation of taking the curl introduces higher order derivatives, which may lead to instabilities in the presence of noise. In [7], the authors have considered the inverse time-harmonic elasticity problem in two dimensions and, after invoking the plane strain hypothesis, developed a stable numerical scheme for solving for the pressure and shear modulus. Their approach derives its stability in part from the transformation of the shear modulus, μ to its log, $v = \log \mu$. In [8], the authors work with the discretized form of the equations of motion and treat them as the equations for the pressure and the shear modulus. Thereafter, they assume that the gradient of the pressure and the shear modulus at the domain boundaries is small and can be neglected and obtain an overdetermined system of equations and solve it using a least-squares formulation. In contrast to the 'direct' approaches described earlier, [9] solves the inverse problem by posing it as a minimization problem and solve it iteratively by utilizing gradient based techniques. The objective function is a measure of the difference between the predicted and a measured displacement field, which is required to satisfy the equations of motion, and the optimization parameters are the spatial values of the material properties. This approach avoids the differentiation of the noisy measured displacement fields, but incurs a higher computational cost, that the authors control through a domain decomposition technique.

The work presented in this manuscript differs from the effort described earlier primarily in the approach used to solve the inverse problem. We develop a weak, or a variational, formulation of the original problem and examine its well-posedness. We conclude that in this regard, it has better properties than the original strong formulation. Thereafter, we present and implement a straightforward finite element discretization of this formulation. Our work builds on our previous effort for the quasi-static inverse elasticity problem [10, 11], where we developed a weak formulation by weighting the original differential equation by its adjoint operating on a weighting function. For the time-harmonic viscoelastic case, we note that we have to work with complex-conjugate of the adjoint operator in order to retain stability. Hence, we dub the new formulation as the complex adjoint weighted equations (CAWE). We consider two special cases of two-dimensional (2D) viscoelasticity not considered elsewhere, namely the anti-plane shear and the plane stress conditions. In the former, the pressure field does not appear in the equations of interest, whereas in the latter, we eliminate the pressure field by utilizing the plane stress condition (we do not assume it to be zero). Finally, we do not rely on boundary data for the shear modulus and the pressure, recognizing that these quantities will be difficult to measure in any practical experiment. The only prescribed data we utilize is the value of the shear modulus measured at one point.

The format of the remainder of the paper is as follows. In Section 2, we present the strong form of the problem we wish to solve and analyze its well-posedness. In Section 3, we present the CAWE and analyze their properties. In Section 4, we present a regularized version of this algorithm. Thereafter in Section 5, we consider a straightforward, finite element based approximation of these equations and present numerical results on synthetic (computer-generated) and experimentally measured data that demonstrate the performance of the method. We end with conclusions in Section 6.

2. PROBLEM FORMULATION

At relatively low frequencies (when the acoustic wavelength is much larger than the domain size), many soft tissues may be modeled as linear, incompressible, isotropic, and viscoelastic materials. For time-harmonic excitation with frequency ω, the equations of motion are then given as follows:

$$\nabla \cdot \boldsymbol{\sigma} + \rho \omega^2 \boldsymbol{u} = \boldsymbol{0}, \tag{1}$$

$$\nabla \cdot \boldsymbol{u} = 0, \tag{2}$$

along with the constitutive equation

$$\boldsymbol{\sigma} = -p\mathbf{1} + 2\mu \boldsymbol{\epsilon}. \tag{3}$$

Here, $\boldsymbol{u}(\boldsymbol{x})$ is the displacement vector, $\boldsymbol{\epsilon}(\boldsymbol{x}) = \frac{1}{2} \left(\nabla \boldsymbol{u} + \nabla \boldsymbol{u}^T \right)$ is the infinitesimal strain tensor, $\boldsymbol{\sigma}(\boldsymbol{x})$ is the stress tensor, $p(\boldsymbol{x})$ is the pressure, ρ is the density (assumed constant here), and $\mu(\boldsymbol{x})$ is the shear modulus. In these equations, all fields, except the constants ρ and ω, are complex variables. A complex, frequency-dependent μ allows the material to be modeled as a viscoelastic material, where the imaginary part of μ is associated with viscous relaxation. In the forward elasticity problem, the material properties μ and ρ and the boundary conditions are specified, and the equations earlier are solved to determine the displacement vector $\boldsymbol{u}$ and the pressure p. In the inverse problem we are considering, the displacement field is specified, and the spatial distribution of the shear modulus is sought.

We consider two 2D approximations of these equations. These are motivated by the fact that in several imaging scenarios, the displacement field is determined on a plane and not in a volume. Thus, some approximation is necessary. As shown in the following paragraphs, in both cases, the problem reduces to: given $\mu(\boldsymbol{x}_0) = \mu_0$ at point $\boldsymbol{x}_0$ find $\mu(\boldsymbol{x})$, for $\boldsymbol{x} \in \Omega$ such that

$$\nabla \cdot \left(\boldsymbol{a}^{(i)} \mu \right) + f^{(i)} = 0, \text{ in } \Omega \qquad i = 1, 2. \tag{4}$$

Anti-plane shear. Here, we assume that the measurements are made in the $x - y$ plane, whereas the displacement is out-of-plane. That is $\boldsymbol{u} = u(x, y)\boldsymbol{e}_z$, where $\boldsymbol{e}_z$ is a unit vector along the $z-$direction. We also assume that the pressure and the shear modulus do not have any out-of-plane variations. With these assumptions, (1) reduces to the scalar Helmholtz equation. That is given the measured field $u(\boldsymbol{x})$, the uniform density ρ and frequency ω determine the modulus $\mu(\boldsymbol{x})$ such that

$$\nabla \cdot (\mu \nabla u) + \rho \omega^2 u = 0. \tag{5}$$

In order to characterize this equation, we consider the corresponding real system of equations obtained for $\boldsymbol{\mu} = [\mu_r, \mu_i]^T$. From (5), we conclude the following:

$$\boldsymbol{G}_{,x} \boldsymbol{\mu}_{,x} + \boldsymbol{G}_{,y} \boldsymbol{\mu}_{,y} + \nabla^2(\boldsymbol{G}) \boldsymbol{\mu} + \rho \omega^2 \boldsymbol{u} = \boldsymbol{0}. \tag{6}$$

Here $\boldsymbol{G} = \begin{bmatrix} u_r & -u_i \\ u_i & u_r \end{bmatrix}$, $\boldsymbol{u} = [u_r, u_i]^T$ and $[\nabla^2(\boldsymbol{G})]_{ij} = \nabla^2 G_{ij}$. The type of the system of PDEs above and hence the required boundary data is determined by the form of the matrix $\boldsymbol{G}$. In particular, when the characteristic equation $\det(\boldsymbol{G}_{,x} - \tau \boldsymbol{G}_{,y}) = 0$ permits real valued τ, the system is hyperbolic. This occurs iff $u_{r,x} u_{i,y} = u_{r,y} u_{i,x}$. Otherwise, the system is elliptic. In most practical cases, we expect the system to be elliptic.

In the applications we are considering, it is highly unlikely that data for μ will be available on the boundaries. Hence, we resort to multiple measured fields in order to determine μ uniquely. We assume that we are given two measured fields $u^{(i)}, i = 1, 2$, and we would like to find a μ that satisfies the equations

$$\nabla \cdot \left(\mu \nabla u^{(i)} \right) + \rho \omega^2 u^{(i)} = 0, \qquad i = 1, 2. \tag{7}$$

These equations may be written as (4), where $\boldsymbol{a}^{(i)} = \nabla u^{(i)}$ and $f^{(i)} = \rho \omega^2 u^{(i)}$.

Plane stress approximation. The plane stress approximation is valid for objects with very small thickness (dimension in the z-direction), where the traction free boundary conditions at the top and bottom surfaces imply that $\sigma_{xz} = \sigma_{yz} = \sigma_{zz} = 0$ is a reasonable assumption throughout. In the time-harmonic case, it also implies that the inertia term in the momentum equation for the z-direction drops out. The zero stress conditions imply that $u_x = u_x(x, y), u_y = u_y(x, y)$

and that $p = 2\mu u_{z,z} = -2\mu(u_{x,x} + u_{y,y})$. Using this expression for pressure in the x and y, momentum equations then yield (4), where $\boldsymbol{a}^{(1)} = [4u_{x,x} + 2u_{y,y}, u_{x,y} + u_{y,x}]^T$ and $\boldsymbol{a}^{(2)} = [u_{x,y} + u_{y,x}, 2u_{x,x} + 4u_{y,y}]^T$ and $f^{(1)} = \rho\omega^2 u_x$ and $f^{(2)} = \rho\omega^2 u_y$.

2.1. Analysis of the strong form

For both anti-plane shear and plane stress approximations, we are lead to solving (4) for the shear modulus. This system has a solution given by $\mu = \mu_h + \mu_p$, where

$$\mu_h(\boldsymbol{x}) = \mu_0 \exp(-\int_{\boldsymbol{x}_p}^{\boldsymbol{x}} \boldsymbol{A}^{-1}(\boldsymbol{x}')\boldsymbol{a}(\boldsymbol{x}') \cdot \mathrm{d}\boldsymbol{x}') \tag{8}$$

$$\mu_p(\boldsymbol{x}) = -\mu_h(\boldsymbol{x}) \int_{\boldsymbol{x}_p}^{\boldsymbol{x}} \frac{\boldsymbol{A}^{-1}(\boldsymbol{x}')\boldsymbol{f}(\boldsymbol{x}')}{\mu^h(\boldsymbol{x}')} \cdot \mathrm{d}\boldsymbol{x}'. \tag{9}$$

This solution exists provided the matrix $\boldsymbol{A} \equiv \boldsymbol{a}^{(1)*} \otimes \boldsymbol{a}^{(1)} + \boldsymbol{a}^{(2)*} \otimes \boldsymbol{a}^{(2)}$ is invertible and $u^{(i)}$ satisfy the following compatibility conditions (Appendix A).

$$\nabla \times (\boldsymbol{A}^{-1}\boldsymbol{a}) = \boldsymbol{0} \tag{10}$$

$$\boldsymbol{C} : \nabla(\boldsymbol{A}^{-1}\boldsymbol{f}) + (\boldsymbol{A}^{-1}\boldsymbol{f}) \cdot \boldsymbol{C}(\boldsymbol{A}^{-1}\boldsymbol{a}) = 0, \tag{11}$$

where $\boldsymbol{a} = \boldsymbol{a}^{(1)*}\nabla \cdot \boldsymbol{a}^{(1)} + \boldsymbol{a}^{(2)*}\nabla \cdot \boldsymbol{a}^{(2)}$, $\boldsymbol{f} = \boldsymbol{a}^{(1)*}f^{(1)} + \boldsymbol{a}^{(2)*}f^{(2)}$ and $\boldsymbol{C} = \begin{bmatrix} 0 & 1 \\ -1 & 0 \end{bmatrix}$. The

superscript $*$ represents the complex-conjugate of a complex field. In practice, $u^{(i)}$ will be corrupted by noise and, hence, it is likely that the compatibility conditions earlier will not be satisfied. Thus a single valued solution of (4) may not exist; in other words, the value of the path integrals in Equation (9) may depend upon the integration path between $\boldsymbol{x}_p$ and $\boldsymbol{x}$. In the next section, we present a weak or a variational formulation of this problem, which overcomes this difficulty by allowing solutions under less restrictive conditions. It also ensures that the weak solution will be equal to the strong solution when the latter exists.

3. COMPLEX ADJOINT WEIGHTED EQUATIONS

The proposed weak form is motivated by our previous work on the quasi-static elasticity problem [11]. In that case, we developed a weak or a variational form by weighting the residual of the original equations by the L_2-adjoint of the differential operator operating on a test function. For the time-harmonic case, we do the same but operate on the complex-conjugate of the test function. This ensures the stability of the formulation.

3.1. Problem formulation

In order to analyze the CAWE formulation, it is convenient to work with a zero specified mean problem instead of a point-specified problem. To this end, we look for a $\hat{\mu}(\boldsymbol{x})$ such that

$$\nabla \cdot \left(\hat{\mu}\boldsymbol{a}^{(i)}\right) + f^{(i)} = 0, \qquad i = 1, 2, \tag{12}$$

with the constraint $\frac{1}{V} \int_{\Omega} \hat{\mu}\mathrm{d}\boldsymbol{x} = \bar{\mu}$, where $V = \mathrm{meas}(\Omega)$. Here, $\bar{\mu}$ is selected such that $\hat{\mu}(\boldsymbol{x}_0) = \mu_0$, which guarantees that $\hat{\mu}(\boldsymbol{x}) = \mu(\boldsymbol{x})$. The equation for specified zero-mean shear modulus $\tilde{\mu}(\boldsymbol{x}) = \hat{\mu}(\boldsymbol{x}) - \bar{\mu}$ is then given by

$$\nabla \cdot \left(\tilde{\mu}\boldsymbol{a}^{(i)}\right) + \tilde{f}^{(i)} = 0, \qquad i = 1, 2, \tag{13}$$

along with the constraint $\frac{1}{V} \int_{\Omega} \tilde{\mu}\mathrm{d}\boldsymbol{x} = 0$. Here, $\tilde{f}^{(i)} = f^{(i)} + \bar{\mu}\nabla \cdot \boldsymbol{a}^{(i)}$. In order to simplify notation from hereon, we suppress the tilde superscript. Thus, the problem we wish to solve is as follows: given $\boldsymbol{a}^{(i)}$ and $f^{(i)}$ find μ such that

$$\nabla \cdot \left(\mu \boldsymbol{a}^{(i)} \right) + f^{(i)} = 0, \qquad i = 1, 2, \text{ in } \Omega, \tag{14}$$

and $\frac{1}{V} \int_{\Omega} \mu \mathrm{d}\boldsymbol{x} = 0$

The CAWE for this problem is given as follows: find $\mu \in \mathcal{V} \equiv \left\{ v \in H^1(\Omega) | \int_{\Omega} v \mathrm{d}\boldsymbol{x} = 0 \right\}$ such that

$$b(w, \mu) = l(w), \forall w \in \mathcal{V}. \tag{15}$$

Here

$$b(w, \mu) = (\nabla w, \boldsymbol{A} \nabla \mu) + (\nabla w, \boldsymbol{a}\mu), \tag{16}$$

$$l(w) = -(\nabla w, \boldsymbol{f}), \tag{17}$$

and $(w, v) = \int_{\Omega} w^* u \, \mathrm{d}\boldsymbol{x}$. Recall, $\boldsymbol{A} = \boldsymbol{a}^{(1)*} \otimes \boldsymbol{a}^{(1)} + \boldsymbol{a}^{(2)*} \otimes \boldsymbol{a}^{(2)}, \boldsymbol{a} = \boldsymbol{a}^{(1)*} \nabla \cdot \boldsymbol{a}^{(1)} + \boldsymbol{a}^{(2)*} \nabla \cdot \boldsymbol{a}^{(2)}$ and $\boldsymbol{f} = \boldsymbol{a}^{(1)*} f^{(1)} + \boldsymbol{a}^{(2)*} f^{(2)}$.

Remark
Another straightforward approach to solving (14) is to look for the function that minimizes the residual of (14) measured in the L_2 norm. This yields the least-squares (LS) formulation: find $\mu \in \mathcal{V}$ such that

$$\sum_{i=1}^{2} Re \left\{ \left(\nabla \cdot (w\boldsymbol{a}^{(i)}), \nabla \cdot (\mu \boldsymbol{a}^{(i)}) + f^{(i)} \right) \right\} = 0, \forall w \in \mathcal{V}. \tag{18}$$

This formulation coincides with the CAWE formulation when $\nabla \cdot \boldsymbol{a}^{(i)} = 0$. In Section 5, we compare the performance of the LS formulation with the CAWE formulation, and in keeping with earlier observations [12], conclude that the LS formulation tends to be overly diffusive.

3.2. Analysis of complex adjoint weighted equation formulation

We now make assumptions on the measured data that determine the well-posedness of the CAWE formulation.

1. We note that by construction, $\boldsymbol{A}(\boldsymbol{x})$ is Hermitian positive semi-definite and thus has non-negative real eigenvalues $\gamma_1(\boldsymbol{x})$ and $\gamma_2(\boldsymbol{x})$. We further assume that these eigenvalues are positive and bounded everywhere in the domain, that is

$$0 < \gamma_0 \leqslant \gamma_1(\boldsymbol{x}), \gamma_2(\boldsymbol{x}) \leqslant \gamma_\infty < \infty. \tag{19}$$

2. Let $q^2(\boldsymbol{x}) = |\nabla \cdot \boldsymbol{a}_1|^2 + |\nabla \cdot \boldsymbol{a}_2|^2$. We assume that q^2 is bounded from above. That is

$$q^2(\boldsymbol{x}) \leqslant q_0^2 < \infty. \tag{20}$$

3. Let C_P be the Poincare constant for Ω. That is, $\|w\|^2 \leqslant C \|\nabla w\|^2, \forall w \in \mathcal{V}, \forall C > C_P$. We assume that the constants γ_0 and q_0 are such that

$$q_0 \sqrt{\frac{C_P}{\gamma_0}} \leqslant 1. \tag{21}$$

Theorem 1
When all these three conditions hold, $b(w, w)$ is coercive and the variational problem (15) has a unique solution.

Proof
Our proof relies on the fact that for $w \in \mathcal{V}$, the H^1 semi-norm $\|\nabla w\|$ defines a norm.

We first prove the coercivity of the bilinear form. From the definition of the bilinear form (16)

$$|b(w,w)| \geqslant Re\{b(w,w)\}$$

$$= (\nabla w, A\nabla w) + Re\left\{(\boldsymbol{a}^{(1)} \cdot \nabla w, (\nabla \cdot \boldsymbol{a}^{(1)})w)\right\}$$

$$+ Re\left\{(\boldsymbol{a}^{(2)} \cdot \nabla w, (\nabla \cdot \boldsymbol{a}^{(2)})w)\right\} \tag{22}$$

For any $\epsilon > 0$

$$Re\left\{(\boldsymbol{a}^{(1)} \cdot \nabla w, (\nabla \cdot \boldsymbol{a}^{(1)})w)\right\} \geqslant -\frac{\epsilon}{2}\|\boldsymbol{a}^{(1)} \cdot \nabla w\|^2 - \frac{1}{2\epsilon}\left\|\left(\nabla \cdot \boldsymbol{a}^{(1)}\right)w\right\|^2 \tag{23}$$

Using this in (22) and recalling that $q^2(\boldsymbol{x}) = |\nabla \cdot \boldsymbol{a}_1|^2 + |\nabla \cdot \boldsymbol{a}_2|^2$, we arrive at

$$|b(w,w)| \geqslant (\nabla w, A\nabla w)\left(1 - \frac{\epsilon}{2}\right) - \frac{1}{2\epsilon}\|wq\|^2 \tag{24}$$

$$\geqslant \|\nabla w\|^2 \gamma_0\left(1 - \frac{\epsilon}{2}\right) - \|w\|^2 \frac{q_0^2}{2\epsilon} \tag{25}$$

$$\geqslant \|\nabla w\|^2 \gamma_0\left(1 - \frac{\epsilon}{2} - \frac{q_0^2 C_P}{2\gamma_0 \epsilon}\right) \tag{26}$$

$$\geqslant \|\nabla w\|^2 \gamma_0\left(1 - q_0\sqrt{\frac{C_P}{\gamma_0}}\right) \tag{27}$$

$$\geqslant C_S\|\nabla w\|^2, \tag{28}$$

where $C_S = \gamma_0\left(1 - q_0\sqrt{\frac{C_P}{\gamma_0}}\right)$. In deriving this relation, in the second line, we have made use of (19) and (20), in the third line, we have used the Poincare inequality, and in the fourth line, we have set $\epsilon = q_0\sqrt{\frac{C_P}{\gamma_0}}$. When (21) is satisfied, the stability parameter $C_S > 0$ and the bilinear form is coercive.

We prove that the bilinear form is bounded as follows,

$$|b(w,\mu)| \leqslant |(\nabla w, A\nabla\mu)| + |(\boldsymbol{a}^{(1)} \cdot \nabla w, (\nabla \cdot \boldsymbol{a}^{(1)})\mu)|$$

$$+ |(\boldsymbol{a}^{(2)} \cdot \nabla w, (\nabla \cdot \boldsymbol{a}^{(2)})\mu)| \tag{29}$$

$$\leqslant \|\nabla w\|\|A\nabla\mu\| + \|\boldsymbol{a}^{(1)} \cdot \nabla w\|\|(\nabla \cdot \boldsymbol{a}^{(1)})\mu\|$$

$$+ \|\boldsymbol{a}^{(2)} \cdot \nabla w\|\|(\nabla \cdot \boldsymbol{a}^{(2)})\mu\| \tag{30}$$

$$\leqslant \gamma_\infty\|\nabla w\|\|\nabla\mu\| + 2\sqrt{\gamma_\infty}q_0\|\nabla w\|\|\mu\| \tag{31}$$

$$\leqslant C_A\|\nabla w\|\|\nabla\mu\|, \tag{32}$$

where $C_A = \gamma_\infty\left(1 + \frac{2q_0\sqrt{C_P}}{\sqrt{\gamma_\infty}}\right)$. In deriving this result, in the second line, we have used the Cauchy-Schwarz inequality, in the third line, we have used (19) and (20), and to get to the final result, we have used the Poincare inequality.

Next we prove that the linear form $l(w)$ is bounded $\forall w \in \mathcal{V}$. From the definition of $l(w)$ (17) we have

$$|l(w)| \leqslant \rho\omega^2 \sum_{n=1}^{2}|\left(\boldsymbol{a}^{(n)} \cdot \nabla w, u^{(n)}\right)| + \mu_0 \sum_{n=1}^{2}|\left(\boldsymbol{a}^{(n)} \cdot \nabla w, \nabla \cdot \boldsymbol{a}^{(n)}\right)| \tag{33}$$

$$\leqslant \rho\omega^2 \sum_{n=1}^{2}\|\boldsymbol{a}^{(n)} \cdot \nabla w\|\|u^{(n)}\| + \mu_0 \sum_{n=1}^{2}\|\boldsymbol{a}^{(n)} \cdot \nabla w\|\|\nabla \cdot \boldsymbol{a}^{(n)}\| \tag{34}$$

$$\leqslant \|\nabla w\|\sqrt{\gamma_\infty}\left(\rho\omega^2 \sum_{n=1}^{2}\|u^{(n)}\| + \mu_0 \sum_{n=1}^{2}\|\nabla \cdot \boldsymbol{a}^{(n)}\|\right) \tag{35}$$

$$\leqslant \|\nabla w\|2\sqrt{\gamma_\infty}\left(\rho\omega^2\sqrt{C_P\gamma_\infty V} + \mu_0 q_0 V\right). \tag{36}$$

Recall that $V = \text{meas}(\Omega)$. In the second line of the previous equation, we have made use of the Cauchy–Schwarz inequality, to get to the third line, we have used (19), and to get to the final result, we have made use of (20) and recognized that $\|u^{(n)}\|^2 \leqslant C_P \|\nabla u^{(n)}\|^2 = C_P \|a^{(n)}\|^2 \leqslant C_P \gamma_\infty V$.

Thus $b(w, \mu)$ is a bounded, coercive bilinear form, and $l(w)$ is a bounded linear from, hence from Lax–Milgram theorem (see for example [13]) the solution to (15) exists and is unique. □

Remark

When only conditions 1 and 2 are satisfied, we can no longer prove that $b(w, w)$ is coercive. However, by making use of Fredholm's alternative, we are guaranteed the existence of a solution. When the corresponding homogeneous problem has no non-trivial solutions, this solution is unique. However, when the homogeneous problem has multiple solutions, our problem too has multiple solutions.

4. REGULARIZATION OF THE COMPLEX ADJOINT WEIGHTED EQUATION FORMULATION

4.1. Motivation for the need for regularization

It is instructive to see when condition 3 is not satisfied because when this occurs, the CAWE formulation loses its uniqueness. For the quasi-static case ($\omega = 0$), steep gradients in the solution μ imply large values of $\nabla \cdot a$ because $a \cdot \nabla \mu + \mu \nabla \cdot a = 0$. Large values of $\nabla \cdot a$ in turn imply a large q_0, which could lead to the violation of condition 3. Thus, in the quasi-static case, we may lose stability near steep gradients in μ. In the time-harmonic case, this may happen even when μ is smooth as described in the following.

For propagating solutions of the Helmholtz equation $u \sim \exp(ik\boldsymbol{n} \cdot \boldsymbol{x})$, where k is the wavenumber and $\boldsymbol{n}$ is the direction of propagation. This yields the estimates $|a| \sim k$, and hence $\gamma_0 \sim |A| \sim k^2$. Further $q_0^2 \sim |\nabla \cdot a|^2 \sim k^4$. In addition, the Poincare constant $C_P \sim L^2$, where L is the characteristic size of the domain. Using these estimates in (21), we note that condition 3 holds when $kL \lesssim 1$. This indicates that the CAWE formulation may cease to be well-posed for problems at high frequencies (domains that are several multiples of the wavelength). Thus we need to regularize the CAWE formulation at large frequencies.

We may also motivate the use of regularization by analyzing the effect of noise. To do this, we write the CAWE as follows:

$$b(w, \mu; \boldsymbol{d}) = l(w; \boldsymbol{d}), \forall w \in \mathcal{V}, \tag{37}$$

where $\boldsymbol{d} = [a^{(1)}, f^{(1)}, a^{(2)}, f^{(2)}]$. In rewriting the original equation this way, we are making the dependence on measured data explicit. In the case of any practical measurement, the data will be tainted by noise $\delta \boldsymbol{d}$. The solution, $\mu + \delta \mu$, will satisfy

$$b(w, \mu + \delta \mu; \boldsymbol{d} + \delta \boldsymbol{d}) = l(w; \boldsymbol{d} + \delta \boldsymbol{d}), \forall w \in \mathcal{V}. \tag{38}$$

Assuming that the noise is small so that all terms that are larger than $O(\delta)$ may be ignored, we use the equations earlier to arrive at an approximate equation for $\delta \mu$,

$$b(w, \delta \mu; \boldsymbol{u}) = D_{\boldsymbol{d}} l(w; \boldsymbol{d}) \cdot \delta \boldsymbol{d} - D_{\boldsymbol{d}} b(w, \mu; \boldsymbol{d}) \cdot \delta \boldsymbol{d}, \forall w \in \mathcal{V}. \tag{39}$$

Using the stability estimate (28), we have

$$C_S \|\nabla \delta \mu\|^2 \leqslant |b(\delta \mu, \delta \mu; \boldsymbol{d})| \leqslant |D_{\boldsymbol{d}} l(\delta \mu; \boldsymbol{d}) \cdot \delta \boldsymbol{d}| + |D_{\boldsymbol{d}} b(\delta \mu, \mu; \boldsymbol{d}) \cdot \delta \boldsymbol{d}|. \tag{40}$$

Or

$$\|\nabla \delta \mu\|^2 \leqslant \frac{|D_{\boldsymbol{d}} l(\delta \mu; \boldsymbol{d}) \cdot \delta \boldsymbol{d}| + |D_{\boldsymbol{d}} b(\delta \mu, \mu; \boldsymbol{d}) \cdot \delta \boldsymbol{d}|}{C_S}, \tag{41}$$

which indicates that $\delta \mu$ may become unbounded when $C_S \to 0$. This will happen when $q_0 \sqrt{\frac{C_P}{\gamma_0}} \to 1$, implying thereby that we need to regularize the problem in this limit.

4.2. Regularized complex adjoint weighted equation

We regularize the CAWE formulation with total variation (TV) regularization [14, 15]. We use TV in order to preserve the sharp changes we expect to see at the interface of two different materials. We implement the TV in the following form:

$$\mathcal{R}[\mu] = \int_{\Omega} \sqrt{|\nabla\mu|^2 + \beta^2}\,\mathrm{d}\Omega. \tag{42}$$

Augmenting CAWE with $D_\mu \mathcal{R}[\mu] \cdot w$ leads to the following weak formulation: find $\mu \in \mathcal{V}$ such that

$$b(w,\mu) + \alpha \mathrm{Re}\left(\nabla w, \frac{\nabla\mu}{\sqrt{|\nabla\mu|^2 + \beta^2}}\right) = l(w), \forall w \in \mathcal{V}. \tag{43}$$

Here, α is the regularization parameter, and β is a parameter selected to ensure that the regularization term is continuous at $\nabla\mu = \mathbf{0}$. We note that the regularization term is non-linear and, as a result, the solution of the problem is also nonlinear.

5. NUMERICAL APPROXIMATION

We approximate the variational problem (15) by approximating the space of functions $\mathcal{V}$ with its finite dimensional counterpart $\mathcal{V}^h \subset \mathcal{V}$. For constructing $\mathcal{V}^h$, we use the standard piecewise constant finite element shape functions. Thus the numerical solution $\mu^h \approx \mu$ satisfies the following variational equation: find $\mu^h \in \mathcal{V}^h$ such that

$$b\left(w^h, \mu^h\right) = l\left(w^h\right), \forall w^h \in \mathcal{V}^h. \tag{44}$$

Because $\mathcal{V}^h \subset \mathcal{V}$, the continuous solution μ also satisfies (44). That is

$$b\left(w^h, \mu\right) = l\left(w^h\right), \forall w^h \in \mathcal{V}^h. \tag{45}$$

Next, we prove that our numerical solution converges at optimal rates to the exact solution under the restrictions of Section 3. We define the error $e = \mu - \mu^h$ and recognize that it is orthogonal to the finite dimensional space of weighting functions. That is subtracting (44) from (45), we have

$$b\left(w^h, e\right) = 0, \forall w^h \in \mathcal{V}^h. \tag{46}$$

We split the error $e = \eta + e^h$, where $\eta = \mu - \mu^i$ and $e^h = \mu^i - \mu^h$. Here, μ^i is the best approximation to μ in the space $\mathcal{V}^h$. It could be, for example, the nodal interpolant of μ. Using the stability estimate, we have

$$
\begin{aligned}
C_S \|\nabla e^h\|^2 &\leqslant |b(e^h, e^h)| \\
&\leqslant |b(e^h, e - \eta)| \qquad \text{(Since } e = \eta + e^h) \\
&\leqslant |b(e^h, \eta)| \qquad\quad \text{(from (46))} \\
&\leqslant C_A \|\nabla e^h\|\|\nabla\eta\| \quad \text{(from (32))}
\end{aligned}
\tag{47}
$$

which yields

$$\|\nabla e^h\| \leqslant \frac{C_A}{C_S}\|\nabla\eta\|. \tag{48}$$

That is, the error in the finite element approximation is of the same order as the error of the best approximation.

We now test the performance of the finite element approximation of the regularized CAWE formulation on synthetically generated data and displacement measurements in tissue mimicking gels. In all cases, we consider anti-plane shear case and work with a non-dimensional version of (7),

where we scale the displacements with a reference value U_{ref}, the shear modulus with a reference value μ_{ref}, and distances with the representative length scale of the domain L. With this non-dimensionalization, these equations transform to

$$\nabla \cdot \left(\mu \nabla u^{(i)} \right) + k^2 L^2 u^{(i)} = 0, \qquad i = 1, 2 \tag{49}$$

where $k = \sqrt{\rho \omega^2 / \mu_{\text{ref}}}$ is the wavenumber. In each case, we use bilinear quadrilateral finite elements to solve the problem.

5.1. Synthetic data

The first problem consists of a rectangular inclusion (denoted by a red rectangle in Figure 1) embedded in a homogeneous background. The shear modulus for the background is $\mu_{\text{bgnd}} = 1 + 0.1i$, that of the inclusion is $\mu_{\text{incl}} = 2.5 + 0.35i$, the wavenumber $kL = 30$, and the domain of the problem is a unit square. These values are selected so that the problem corresponds to a likely scenario in elasticity imaging of tissue.

We solve the forward problem of anti-plane shear using a uniform mesh of 100×100 finite elements. We model the infinite domain using the perfectly matched layers described in [16]. We consider two point sources placed at the bottom left and the top left corners (Figure 1). These yield the two 'measured' displacement fields $u^{(1)}$ and $u^{(2)}$. We calculate the derivatives of these fields by solving the variational problems

$$\left(\boldsymbol{w}^h, \boldsymbol{a}^{(i)} \right) = \left(\boldsymbol{w}^h, \nabla u^{(i)} \right), \qquad i = 1, 2. \tag{50}$$

This yields $\boldsymbol{a}^{(i)}$ on a piecewise continuous finite element basis. In order to evaluate $\nabla \cdot \boldsymbol{a}^{(i)}$, we simply take the derivative of $\boldsymbol{a}^{(i)}$ within each element.

We note that although the fields $u^{(i)}$ are the same in the forward and the inverse problems, their gradients are not the same. For the forward problem, the gradient fields are $\nabla u^{(i)}$, whereas for the inverse problem, they are the L_2 projection of $\nabla u^{(i)}$ on to a piecewise continuous finite element basis (50). Thus even for the case with no noise, we are not committing the so-called inverse crime.

We use the synthetically created measured data $u^{(i)}$, $\boldsymbol{a}^{(i)}$ and $\nabla \cdot \boldsymbol{a}^{(i)}$ to reconstruct the shear modulus in a subset of the original domain, as indicated by the square in Figure 1. We work with the reduced domain so that there are no sources present in the region of reconstruction. In this figure, we also indicate the extent of the inclusion with a red rectangle. We use a mesh of 40×40 elements for the inverse problem. We fix the shear modulus value at the origin to the correct value of the background, that is $1 + 0.1i$. We note that even though there is no explicit noise in the data, the numerical differentiation of $u^{(i)}$ introduces noise, and this effect is clearly seen in the reconstructions.

In Figure 2, we have shown the reconstruction using the CAWE formulation. From the plot of the real part of μ, we observe that we recover the shape and the location of the inclusion well. We also recover the value of the modulus in the background and in the inclusion accurately. There are, however, some artifacts that are introduced through the noise in the derivatives of the measured data.
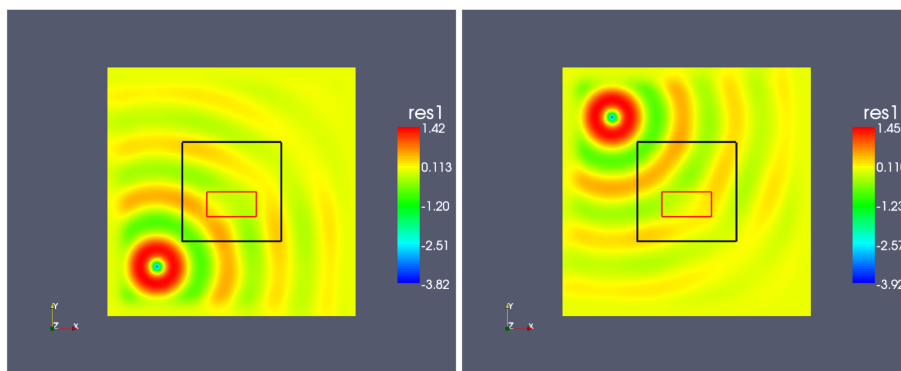

Figure 1. Real part of the wave fields used for the inverse problem.

These are in the form of wavy variations in the background and the inclusion and as overshoots at the interface. These artifacts are more obvious in the image of the imaginary part of the shear modulus, where they tend to overwhelm the entire image. We note that the amplitude of these variations is about the same for the real and the imaginary components of the shear modulus. They are seen
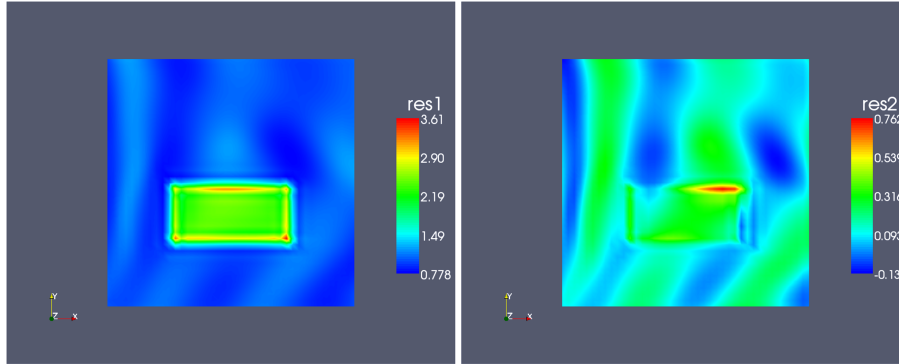

Figure 2. Reconstruction of the shear modulus using CAWE with zero-noise displacement fields. Left: real component; right: imaginary component.
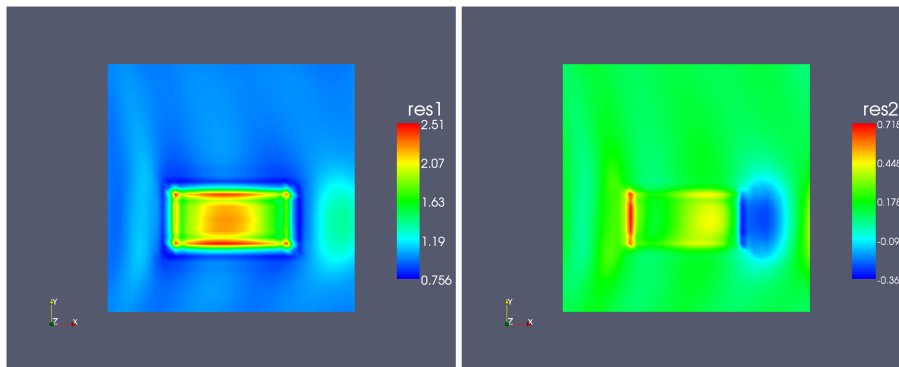
Figure 3. Reconstruction of the shear modulus using least squares with zero-noise displacement fields. Left: real component; right: imaginary component.
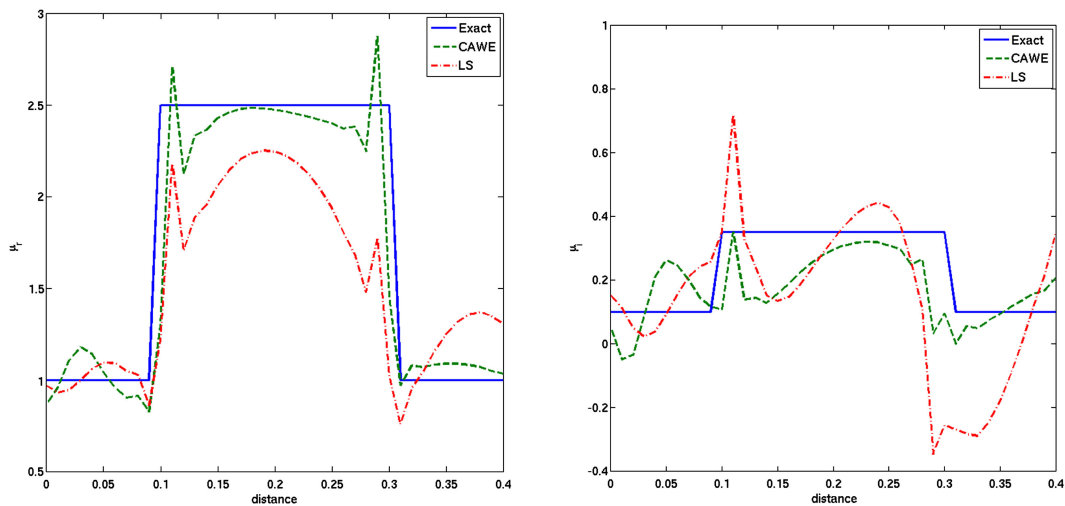
Figure 4. Variation of material properties along a horizontal line through the center of the inclusion with no noise and regularization. Left: real component; right: imaginary component.

more clearly in the latter because the absolute value of the latter is smaller. In Figure 4, we have plotted the variation in the reconstructed shear modulus along a horizontal line running through the center of the inclusion. This plot reaffirms the observations made in this paragraph.

In order to compare the performance of the CAWE formulation, we solve the same problem using an LS formulation. This formulation is given by (18) in Section 3. The reconstructions are shown in Figure 3. The measured data is exactly the same as that used for the CAWE formulation. We observe that LS formulation has similar artifacts and that they appear to be stronger. Also, the contrast between the inclusion and the background appears to be underestimated, and the variations within these regions (which are homogeneous) appear to be stronger. This is clearly seen in the plot of the material properties along a horizontal line through the center of the inclusion (Figure 4).

In Figures 5–7, we present results for the CAWE and LS formulations using the same data, but with TV regularization. The regularization parameter $\alpha = 100$ was the same for both cases. For the CAWE formulation, we observe that the shape of the inclusion is captured accurately, and there is an error of about 0.15 units in the contrast. However, the overshoots and undershoots at the very sharp interface between the inclusion at the background persist. In comparison, the LS formulation is more inaccurate. The error in the contrast is about 0.5 units, there are variations in the background and (especially) the inclusions, and there are sharp oscillations at the interface. We also note that LS solutions tend to be 'diffusing' away from the sources, which are located on the left edge.

Next, we add 3% Gaussian white noise to the displacement fields and test the performance of the algorithms. The regularization parameter $\alpha = 1000$, and all other aspects of the reconstructions are unchanged. We remark that in evaluating the derivatives of the displacement fields, we do not perform any smoothing. Instead, we rely on the regularization term to provide all the necessary smoothing. The reconstruction for the CAWE formulation is shown in Figure 8. We observe that the
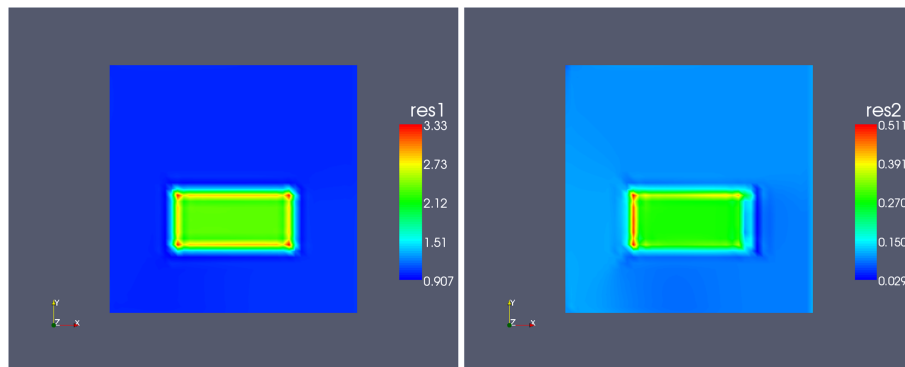

Figure 5. Reconstruction of the shear modulus using complex adjoint weighted equation with zero-noise displacement fields ($\alpha = 100$). Left: real component; right: imaginary component.
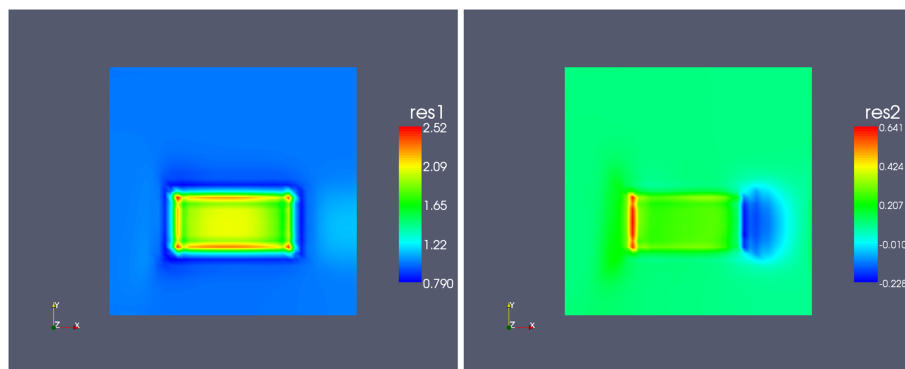

Figure 6. Reconstruction of the shear modulus using least squares with zero-noise displacement fields ($\alpha = 100$). Left: real component; right: imaginary component.
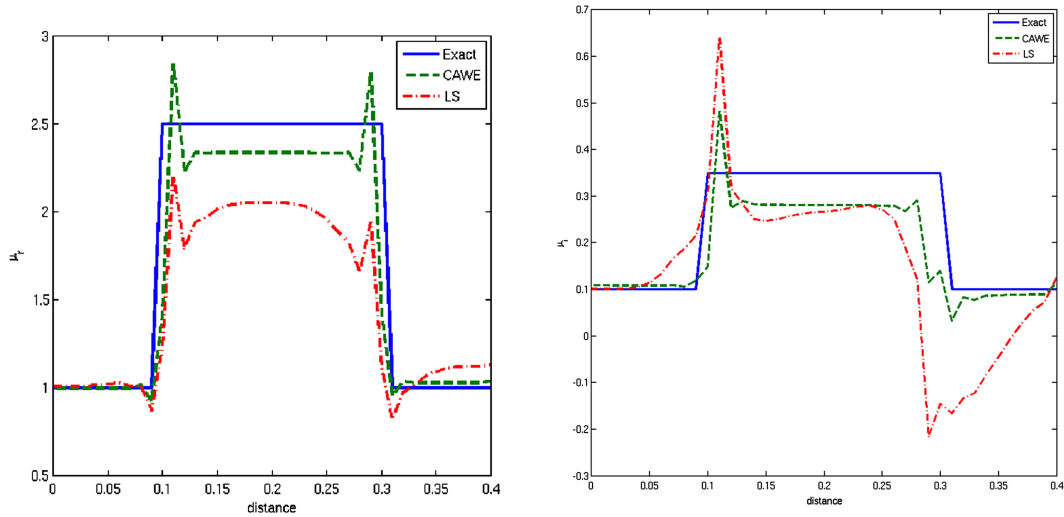
Figure 7. Variation of material properties along a horizontal line through the center of the inclusion with no noise and $\alpha = 1.0e2$. Left: real component; right: imaginary component.
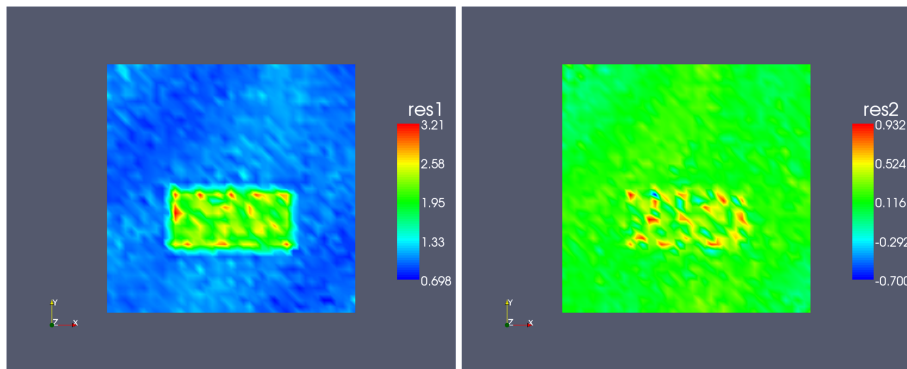

Figure 8. Reconstruction of the shear modulus using complex adjoint weighted equation with noisy displacement fields ($\alpha = 1000$). Left: real component; right: imaginary component.

shape and the location of the inclusion is recovered well, whereas the contrast in the real component is diminished by about 20%. This is to be expected because of the higher value of the regularization parameter. We also observe that the background and the inclusion now have sharp oscillations. These may be tempered somewhat, at the expense of losing contrast, by increasing the regularization parameter. We remark that although the reconstruction of the imaginary part of the modulus looks much poorer when compared with the real part, the magnitude of the error in both is about the same. We observe that the LS results in this case are completely incorrect (Figure 9). They tend to decay uniformly away from the left edge where the sources and the Dirichlet data for μ is specified. The comparison between the CAWE and LS reconstructions are shown in Figure 10.

5.2. Gelatin phantom

In this section, we apply the CAWE formulation to determine the shear modulus of a tissue-mimicking gelatin phantom using experiments performed at the Mayo clinic [17, 18]. The sample consists of two cylindrical inclusions embedded in a homogeneous background. The diameters of the inclusions are 16 and 3 mm. The inclusions and the background were constructed using different gelatin concentrations in order to achieve a contrast in material properties. The shear modulus was estimated to be 20($\pm$3) kPa in the background and 130($\pm$10) kPa in the inclusions using a local frequency estimation technique [17]. The details of the experiment are described in [18].
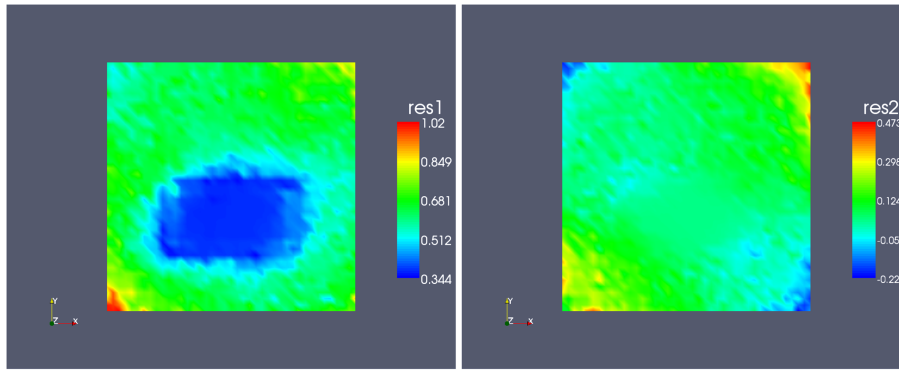
Figure 9. Reconstruction of the shear modulus using least squares with noisy displacement fields ($\alpha = 1000$). Left: real component; right: imaginary component.
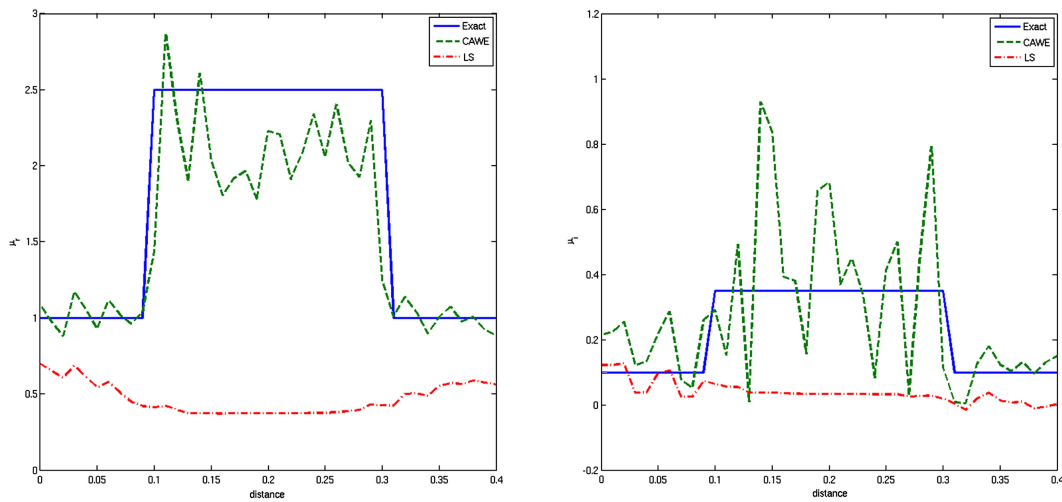

Figure 10. Variation of material properties along a horizontal line through the center of the inclusion with 3% noise and $\alpha = 1.0e3$ Left: real component; right: imaginary component.

The specimen was excited using a harmonic mechanical force and the three-dimensional time-harmonic displacements were measured by a phase-contrast MRI sequence with special cyclic motion encoding gradients [1]. The mechanical force was applied at the surface of the phantom via a contact plate, which oscillates in the out-of-plane direction, parallel to the axes of the cylindrical inclusions. This configuration approximated the state of anti-plane shear discussed in Section 2. The excitation frequency was 300 Hz. The imaging plane consisted of 200×160 pixels of size 0.6275×0.6275 mm^2. Displacements were measured at eight time instances. This data was transformed to the frequency domain to obtain displacement at the driving frequency, $\omega = 2\pi \times 300$ rad/s. The density of gelatin was assumed to be $\rho = 1000$ kg/m^3.

With the discussion on anti-plane shear in Section 2, we expect that the shear modulus satisfies an elliptic boundary value problem. Hence, we require data for the shear modulus on the entire boundary of the domain of interest. The value of the shear modulus on the boundary was determined by fitting a plane wave in the lower, homogeneous, region of the phantom to first estimate the wavenumber and then the shear modulus. It was found that $\mu = (20. + i\,0.5)$ kPa provided a good fit. This value was used as boundary data.

The measured displacement data was smoothed using a quadratic LS filter. This filter performed an LS fit of the displacement on to a quadratic surface (with $1, x, y, xy, x^2, \& y^2$ monomials) over 4×4 window, and thus generated smooth displacements and strains.

The problem was non-dimensionalized with $\mu_{\text{ref}} = 20$ kPa, $U_{\text{ref}} = 1.32 \times 10^{-4}$ m and $L = L_x = 0.0998$ m. This led to a wavenumber of $kL = 42$. The non-dimensionalized smoothed displacement field in the out-of-plane direction is shown in Figure 11. In this figure, we can clearly observe the scattering of the wave by the larger of the two inclusions. The effect of the smaller inclusion is not seen in this figure.

The boundary data, along with the smoothed displacement and strain data, were used in the regularized CAWE algorithm in order to evaluate the complex shear modulus. The reconstruction was performed on the same mesh as the displacement measurement. Only the real part of the shear modulus was recovered because the imaginary part was much smaller in comparison.

In a typical inverse problem, the regularization parameter may be determined using either Morozov's discrepancy principle or the *L*-curve (e.g., [19]). Morozov's principle requires a precise estimate of measurement noise in an appropriate norm, which is not available to us. Further, we have found that the *L*-curve tends not to work well in conjunction with TV regularization. Instead of these, we have used a priori information in order to select the value of the parameter. In particular, because we know that the background is homogeneous, we have selected the smallest value of the regularization parameter, which yields a roughly uniform background.

The result, obtained with the regularization parameter $\alpha = 4000$ is shown in Figure 12. In this figure, both inclusions are seen quite clearly. The shape of the inclusions is also recovered, although a portion of the larger inclusion, which is in the 'shadow' of the incident wave, is somewhat diminished. In this region, the displacement magnitude is small and, as a result, the ratio of the
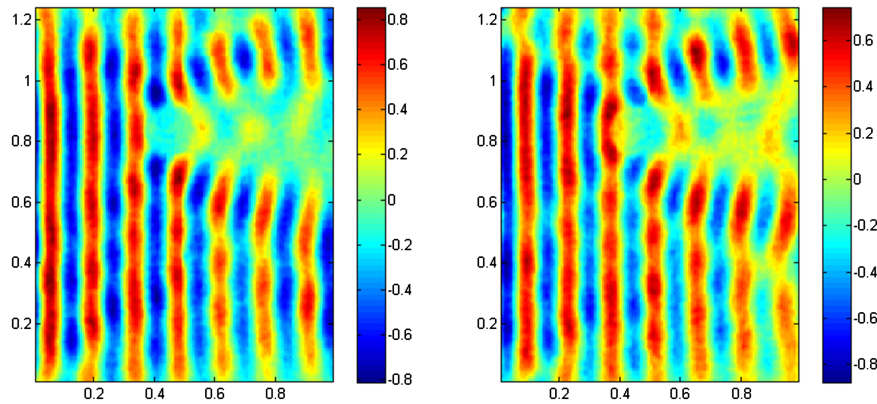

Figure 11. Out-of-plane component of the smooth displacement field. Left: real component; right: imaginary component.
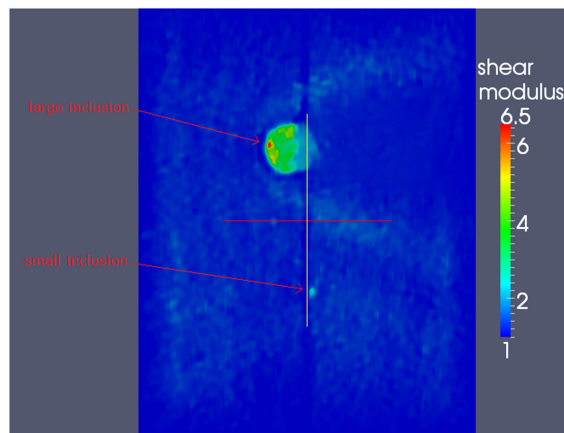

Figure 12. Reconstruction of the real component of the shear modulus for the gelatin phantom using complex adjoint weighted equation with the displacement field ($\alpha = 4000$).
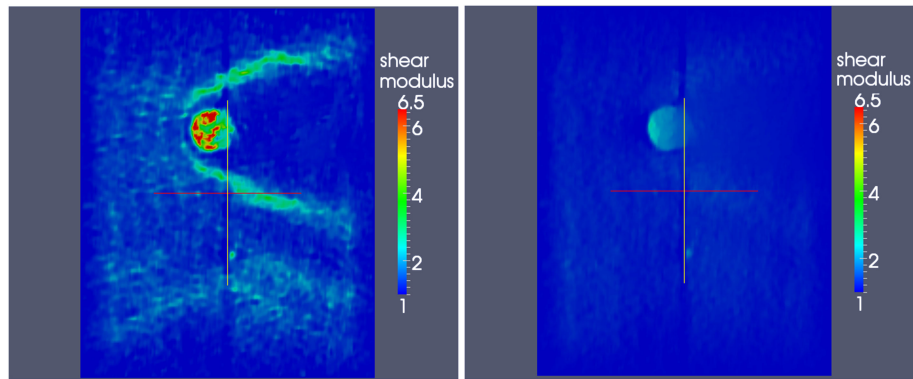
Figure 13. Reconstruction of the real component of the shear modulus for the gelatin phantom using complex adjoint weighted equation with the displacement field. Left: $\alpha = 2000$; right: $\alpha = 8000$.

regularization term to the data matching term in (43) is large. Consequently, the effect of the regularization term is greater, which leads to a reduced contrast between the inclusion and the background. This makes the inclusion appear incomplete. This may be overcome by selecting a regularization parameter that is proportional to the local magnitude of the data matching term and, hence, maintains the same ratio between the data matching and regularization terms.

The contrast in the shear modulus between the large inclusion and the background is about five, whereas for the smaller inclusion, it is around three. The actual value (obtained from an independent test) is around 6.5 for both. For the large inclusion, this translates to an error of about 20%, which may be attributed to the tendency of the TV regularization to reduce the total variation, and hence the contrast in the image. The additional loss in contrast for the smaller inclusion may be attributed to the spatial smoothing of the displacement field. We note that we have employed a window of 4×4 pixels for this smoothing, and thus we expect it to have a significant effect on the small inclusion, which is only about 5 pixels in diameter.

It is worth noting that in this example, using magnetic resonance elastography and the CAWE method, we are able to detect an inclusion as small as 3 mm in diameter. This has implications in the early detection of breast cancer, in particular, in the detection of ductal carcinoma *in situ*, which is typically small in size as it is confined to a single milk duct.

The effect of varying the regularization parameter, α, is displayed in Figure 13, where we have plotted reconstructions obtained with $\alpha = 2000$ and $\alpha = 8000$, which correspond to half and two times, respectively, the value used in Figure 12. We note that with decreasing α, the contrast in the inclusions increases. However, this also leads to spurious oscillations in the background.

6. CONCLUSIONS

We have considered the problem of determining the spatial distribution of the complex-valued shear modulus within an incompressible linear viscoelastic solid undergoing infinitesimal, time-harmonic deformation, from the knowledge of the displacement field in its interior. We have restricted our attention to the 2D problems of anti-plane shear and plane stress. For both these cases (two measurements for anti-plane shear and one for plane stress), the shear modulus is required to satisfy two independent inverse Helmholtz equations. These equations permit the existence of a strong solution given that the measured data satisfy compatibility equations that are unlikely to hold for noisy measurements.

We have addressed this issue by formulating a weak, or a variational, formulation of these equations, which is obtained by weighting the original partial differential equation by its adjoint operating on the complex-conjugate of an arbitrary weighting function. We term this formulation

the CAWE. We prove that these equations lead to a well-posed variational problem under less restrictive conditions on the measured data. However, at high frequency, or with rough data, they too may become ill-posed. For this reason, we append to our formulation a regularization term.

We have developed a numerical method from the regularized CAWE formulation by restricting the function spaces to standard, bilinear finite element function spaces. We have tested the performance of this method on synthetically generated data and experimentally measured data. The method successfully reconstructs real and imaginary parts of shear modulus from simulated data with 3% added noise, and further successfully reconstructs the real part of the shear modulus from measured data.

APPENDIX A

Equations for μ are

$$\boldsymbol{a}^{(i)} \cdot \nabla \mu + \mu \nabla \cdot \boldsymbol{a}^{(i)} + f^{(i)} = 0, \qquad i = 1, 2. \tag{A.1}$$

Multiplying these by $\boldsymbol{a}^{(i)*}$ and adding the resulting equations, we arrive at

$$\boldsymbol{A} \cdot \nabla \mu + \boldsymbol{a}\mu + \boldsymbol{f} = \boldsymbol{0}. \tag{A.2}$$

The solution to this equation is given by the sum of a homogeneous and a particular part $\mu = \mu^h + \mu^p$, where the equation for μ^h is

$$\nabla \mu^h + \boldsymbol{A}^{-1} \boldsymbol{a} \mu^h = \boldsymbol{0}. \tag{A.3}$$

We write $\mu^p = \mu^h g$, which yields the following equation for g,

$$\nabla g + \frac{\boldsymbol{A}^{-1} \boldsymbol{f}}{\mu^h} = \boldsymbol{0}. \tag{A.4}$$

The solution to (A.3) and (A.4) yield,

$$\mu^h(\boldsymbol{x}) = \mu_0 \exp(-\int_{\boldsymbol{x}_p}^{\boldsymbol{x}} \boldsymbol{A}^{-1}(\boldsymbol{x}') \boldsymbol{a}(\boldsymbol{x}') \cdot \mathrm{d}\boldsymbol{x}') \tag{A.5}$$

$$\mu^p(\boldsymbol{x}) = -\mu^h(\boldsymbol{x}) \int_{\boldsymbol{x}_p}^{\boldsymbol{x}} \frac{\boldsymbol{A}^{-1}(\boldsymbol{x}') \boldsymbol{f}(\boldsymbol{x}')}{\mu^h(\boldsymbol{x}')} \cdot \mathrm{d}\boldsymbol{x}' \tag{A.6}$$

Taking the curl of (A.3) yields the compatibility condition for μ^h to exist, viz.

$$\nabla \times (\boldsymbol{A}^{-1} \boldsymbol{a}) = \boldsymbol{0}. \tag{A.7}$$

Taking the curl of (A.4) and eliminating μ^h using (A.3) yields the following compatibility condition for μ^p to exist

$$\boldsymbol{C} : \nabla(\boldsymbol{A}^{-1} \boldsymbol{f}) + (\boldsymbol{A}^{-1} \boldsymbol{f}) \cdot \boldsymbol{C} (\boldsymbol{A}^{-1} \boldsymbol{a}) = 0, \tag{A.8}$$

where $\boldsymbol{C} = \begin{bmatrix} 0 & 1 \\ -1 & 0 \end{bmatrix}$.

REFERENCES

1. Muthupillai R, Lomas DJ, Rossman PJ, Greenleaf JF, Manduca A, Ehman RL. Magnetic resonance elastography by direct visualization of propagating acoustic strain waves. *Science* 1995; **269**:1854–1857.

2. Parker KJ, Taylor LS, Gracewski S, Rubens DJ. A unified view of imaging the elastic properties of tissue. *The Journal of the Acoustical Society of America* 2005; **117**:2705–2712.

3. Sinkus R, Tanter M, Xydeas T, Catheline S, Bercoff J, Fink M. Viscoelastic shear properties of *in vivo* breast lesions measured by MR elastography. *Magnetic Resonance Imaging* 2005; **23**(2):159–165.

4. Kass L, Erler JT, Dembo M, Weaver VM. Mammary epithelial cell: influence of extracellular matrix composition and organization during development and tumorigenesis. *International Journal of Biochemistry and Cell Biology* 2007; **39**(11):1987–1994.

5. Samani A, Zubovits J, Plewes D. Elastic moduli of normal and pathological human breast tissues: an inversion-technique-based investigation of 169 samples. *Physics in Medicine and Biology* 2007; **52**:1565–1576.

6. Oliphant TE, Manduca A, Ehman RL, Greenleaf JF. Complex-valued stiffness reconstruction for magnetic resonance elastography by algebraic inversion of the differential equation. *Magnetic Resonance in Medicine* 2001; **45**(2):299–310.

7. McLaughlin JR, Zhang N, Manduca A. Calculating tissue shear modulus and pressure by 2D log-elastographic methods. *Inverse Problems* 2010; **26**:085007.

8. Park E, Maniatty A. Shear modulus reconstruction in dynamic elastography: time-harmonic case. *Physics in Medicine and Biology* 2006; **51**:3697–3721.

9. Van Houten EEW, Paulsen KD, Miga MI, Kennedy FE, Weaver JB. An overlapping subzone technique for MR-based elastic property reconstruction. *Magnetic Resonance in Medicine* 1999; **99**:779–786.

10. Albocher U, Oberai AA, Barbone PE, Harari I. Adjoint-weighted equation for inverse problems of incompressible plane-stress elasticity. *Computer Methods in Applied Mechanics and Engineering* 2009; **198**(30-32):2412–2420.

11. Barbone PE, Rivas CE, Harari I, Albocher U, Oberai AA, Zhang Y. Adjoint-weighted variational formulation for the direct solution of inverse problems of general linear elasticity with full interior data. *International Journal for Numerical Methods in Engineering* 2010; **81**(13):1713–1736.

12. Barbone PE, Oberai AA, Harari I. Adjoint-weighted variational formulation for a direct computational solution of an inverse heat conduction problem. *Inverse Problems* 2007; **23**:2325–2342.

13. Brenner SC, Scott LR. *The Mathematical Theory of Finite Element Methods*. Springer Verlag: New York, 2008.

14. Rudin LI, Osher S, Fatemi E. Nonlinear total variation based noise removal algorithms. *Physica D: Nonlinear Phenomena* 1992; **60**(1-4):259–268.

15. Vogel CR, Oman ME. Fast, robust total variation-based reconstruction of noisy, blurred images. *Image Processing, IEEE Transactions on* 2002; **7**(6):813–824.

16. Turkel E, Yefet A. Absorbing PML boundary layers for wave-like equations. *Applied Numerical Mathematics* 1998; **27**(4):533–557.

17. Manduca A, Muthupillai R, Rossman PJ, Greenleaf JF, Ehman RL. Image processing for magnetic resonance elastography. *In Proceedings of SPIE* 1996; **2710**:616–623.

18. Romano AJ, Bucaro JA, Ehnan RL, Shirron JJ. Evaluation of a material parameter extraction algorithm using MRI-based displacement measurements. *Ultrasonics, Ferroelectrics and Frequency Control, IEEE Transactions on* 2000; **47**(6):1575–1581.

19. Vogel CR. *Computational Methods for Inverse Problems*. SIAM: Philadelphia, 2002.